ARTICLE

SABRE Enhancement with Oscillating Pulse Sequences

Xiaoqing Li, *a Jacob R. Lindale b, Shannon L. Erikssonan c and Warren S. Warren *a, b, d

Received 00th January 20xx, Accepted 00th January 20xx

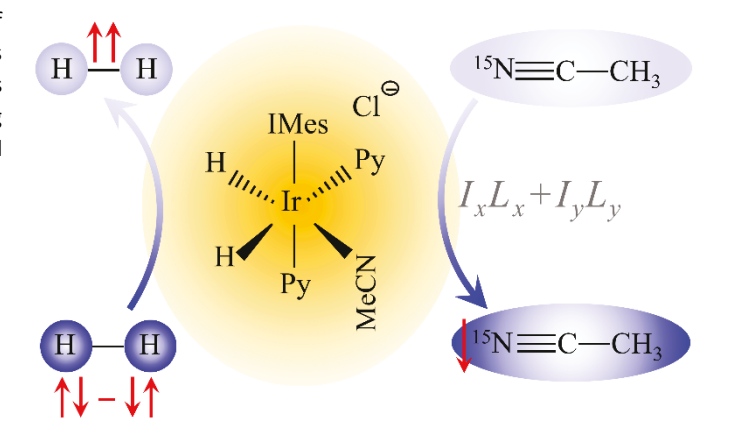
DOI: 10.1039/x0xx00000x

SABRE (Signal Amplification by Reversible Exchange) methods provide a simple, fast, and cost-effective method to hyperpolarize a wide variety of molecules in solution, and have been demonstrated with protons and, more recently, with heteronuclei (X-SABRE). Here, we present several oscillating pulse sequences that use magnetic fields far away from the resonance condition of continuous excitation and can commonly triple the polarization. An analysis with average Hamiltonian theory indicates that the oscillating pulse, in effect, adjusts the J-couplings between hydrides and target nuclei and that a much weaker coupling produces maximum polarization. This theoretical treatment, combined with simulations and experiment, show substantial magnetization improvements relative to traditional X-SABRE methods. It also shows that, in contrast to most pulse sequence applications, waveforms with reduced time symmetry in the toggling frame make magnetization generation more robust to experimental imperfections.

Introduction

Low sensitivity is an intrinsic limitation of nuclear magnetic resonance, because the energy difference caused by Zeeman splitting is normally much smaller than thermal energy, and the resultant equilibrium fractional magnetization is low (P $\sim 10^{-5}$ -10⁻⁶). Hyperpolarization methods derive spin order from other sources and can create significantly higher magnetization. Three major methods have evolved over the last several decades: dissolution dynamic nuclear polarization (d-DNP),1 which derives nuclear spin order from unpaired electrons, and spin exchange optical pumping (SEOP),2 which derives it indirectly from circularly pumped optical transitions and hydrogenative para-hydrogen-induced polarization (PHIP),3,4 which derives spin order from para-hydrogen, the singlet isomer of the H2 molecule. Active research continues on all of these methods, in large part because they have obvious limitations. SEOP is restricted to a few noble gases, d-DNP needs high-cost hyperpolarization hardware and a long hyperpolarization time (often an hour or so for ¹³C and ¹⁵N), and PHIP requires a proper precursor molecule and catalyst.

More recently, a variety of methods have evolved which use reversible interactions of parahydrogen and a target molecule with an iridium catalyst, starting with the method known as Signal Amplification By Reversible Exchange (SABRE).⁵⁻⁸ Both parahydrogen and target substrate rapidly and reversibly exchange with sites on the catalyst metal centre. In a low magnetic field (~6mT), J-couplings between the hydrides and protons on the bound species transfer spin order between them, and this makes it possible to spontaneously create excess magnetization on the target protons. In recent years, a variety of extended SABRE methods (X-SABRE)⁹⁻¹⁶ have relaxed the experimental restrictions. For example, SABRE-SHEATH (Scheme 1) (Signal Amplification by Reversible Exchange in



Scheme 1. Schematic representation of generation of hyperpolarized ¹⁵N labelled acetonitrile. IMes, Py and MeCN represent [1,3-bis(2,4,6-trimethyphenyl)-imidazoyl], pyridine ligands, and acetonitrile, respectively.

^a Department of Physics, Duke University Durham, NC 27708 (USA). E-mail: xiaoqina.li@duke.edu

b. Department of Chemistry, Duke University Durham, NC 27708 (USA).

^{c.} School of Medicine, Duke University Durham, NC 27708 (USA).

^d Department of Biomedical Engineering, and Radiology, Duke University, Durham, NC (27708) (USA). E-mail: warren.warren@duke.edu

[†] Footnotes relating to the title and/or authors should appear here. Electronic Supplementary Information (ESI) available: [details of any supplementary information available should be included here]. See DOI: 10.1039/x0xx00000x

SHield Enables Alignment Transfer to Heteronuclei) has permitted direct targeting of heteronuclei (^{15}N , ^{13}C , ^{19}F , and ^{31}P) $^{9,\ 17\cdot21}$ with much longer T_1 values than 1H . In this case, the optimal magnetic field is about $0.6\mu T$, 22 so the experiments are generally done in a magnetic shield. Other X-SABRE methods have been adapted to transfer spin order from parahydrogen directly in a high field magnet. $^{12\cdot16}$

SABRE and X-SABRE are simpler, faster, and less expensive than commercially available hyperpolarization methods, and more general than PHIP. However, the amount of polarization produced at any one time is generally lower than with d-DNP or SEOP, although there is no fundamental reason why this must be true. We have recently shown²³ that a big part of the reason is that the novel field regime for SABRE and X-SABRE (where even heteronuclear couplings can be readily interconverted between the strong and weak coupling limits), combined with the very complex exchange dynamics, imply that the method is theoretically underexplored; there are clearly better (but nonintuitive) approaches to creating polarization than a simple continuous field. Specifically, reference [23] shows that an alternating two-field pulse sequence (both fields high, but with a small average) can produce very large SABRE enhancements. In fact, two papers on similar field manipulations were submitted shortly after that work. ^{24, 25}

This paper more systematically explores the use of periodic field perturbations (Fig. 1), with the goal of creating enhanced magnetization with low sensitivity to experimental imperfections such as field inhomogeneity. It exploits a major advantage of operating in the low field regime: the ability to change the main magnetic field at will, much faster than any couplings, using very simple hardware. In particular, we obtain general insight from average Hamiltonian theory^{26, 27} and then do highly accurate calculations using an exact dissipative master equation treatment.²⁸ In all cases, optimal pulse sequences look nonintuitive and do not

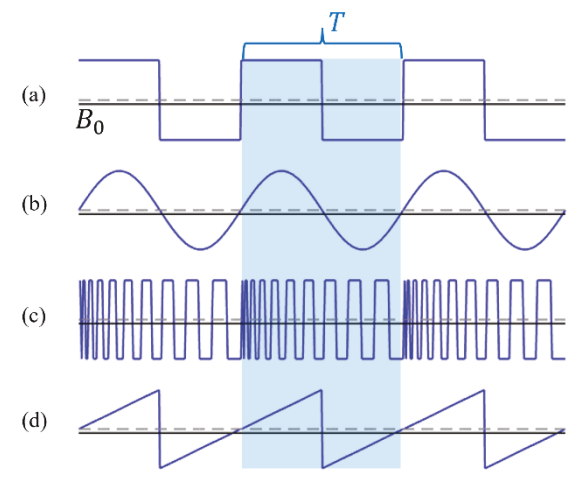


Fig. 1 Pulse sequences for enhanced SABRE/X-SABRE excitation. (a) square pulse, (b) sine wave pulse, (c) chirped pulse, and (d) ramp pulse. The dashed grey line refers to zero magnetic field, and the black line is an offset field, B_0 . As shown in this paper, all of these sequences are capable of producing signal enhancements (relative to a constant field) but the lower symmetry sequences (c) and (d) have practical advantages.

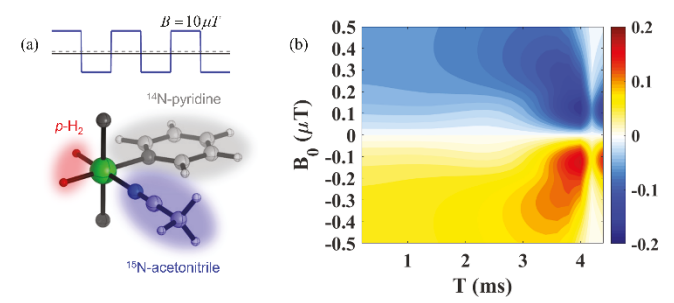


Fig. 2 (a) Schematic representation of the pulse and the spin system used in simulation. The coupling strength between the two hydrides is $J_{HH}=-8H$. It is often a good approximation to assume that the ligand is only coupled to one of the two hydrides, and the strength is $J_{HL}=-25Hz$. (b) Final 15N polarization level simulated with the unbalanced square wave. The offset field B_0 is varied from $-0.5\mu T$ to $0.5\mu T$, and the pulse period T is scanned in the range of 0 to 4.4ms, while the pulse amplitude B is fixed at $10\mu T$. Simulation parameters: 100% parahydrogen, $k_L=24s^{-1}$, $k_H=8s^{-1}$, [catalyst]: [ligand]=1:10. A pulse with $B_0=\pm 0.13\mu T$ and T=4ms yields the maximum ~18% polarization, which is much larger than the continuous wave counterpart ~5%.

match continuous excitation, either in their peak or average field strength. Fig. 2 shows one example; in this system, experimentally and in simulations the maximal magnetization (~5%) is generated with a continuous ~0.6 μ T field, but far larger magnetization (~18%) is produced by a correctly timed square wave offset from a zero average field by about one-fifth that value (~0.13 μ T). We will also show that, in contrast to most pulse sequence applications, waveforms with reduced time symmetry in the toggling frame (such as the last two sequences in Fig. 1) make magnetization generation more robust to experimental imperfections.

Theoretical Perspective on Oscillating Pulses

Each pulse sequence in Fig. 1 consists of a low offset field (<1 μ T) and an oscillating pulse with alternating positive-negative amplitude (10-100 μ T). Every pulse is specified by three parameters--the offset field B₀, the oscillating field B(t), and the pulse period T. We describe these sequences using average Hamiltonian theory, ^{26,27} which relies on the principle that under suitable conditions, the evolution of a spin system driven by a time-dependent external field can be described by the average effect of the field over one cycle of its oscillation. For the sake of comprehensiveness, we analyse both AA'B 3-spin system and AA'BB' 4-spin system (shown in SI section 3). The full Hamiltonian of the three-spin AA'B system is expressed in equation (1)

$$\begin{split} \widehat{\mathcal{H}}_{prime}(t) &= - \big(B_0 + B(t) \big) \big(\gamma_H \big(\hat{l}_{1z} + \hat{l}_{2z} \big) + \gamma_L \hat{L}_z \big) \\ &+ 2\pi J_{HH} \big(\vec{l}_1 \cdot \vec{l}_2 \big) + 2\pi J_{HL} \big(\vec{l}_1 \cdot \vec{L} \big) \end{split} \tag{1}$$

here in natural units ($\hbar=1$). The spin operator of the target nuclei is labelled as \vec{L} , and the two hydride spins are \vec{I}_1 and \vec{I}_2 . We can rearrange this Hamiltonian as:

$$\widehat{\mathcal{H}}_{rearranged}(t) = -(B_0 + B(t))\gamma_H(\widehat{I}_{1z} + \widehat{I}_{2z} + \widehat{L}_z) + (\Delta\omega_0 + \Delta\omega(t))\widehat{L}_z + 2\pi J_{HH}(\vec{I}_1 \cdot \vec{I}_2) + 2\pi J_{HL}(\vec{I}_1 \cdot \vec{L})$$
(2)

in which $\Delta\omega_0=B_0(\gamma_H-\gamma_L)$ and $\Delta\omega(t)=B(t)(\gamma_H-\gamma_L)$ are the Larmor frequency differenCe between hydrides and the target nuclei caused by the offset field and the oscillating pulse respectively. The first term in equation (2) which is directly proportional to the z component of the total spin angular momentum can be ignored since it commutes with the rest of the Hamiltonian, giving a simplified Hamiltonian of the form

$$\widehat{\mathcal{H}}(t) = (\Delta\omega_0 + \Delta\omega(t))\widehat{L}_z + 2\pi J_{HH}(\vec{I}_1 \cdot \vec{I}_2) + 2\pi J_{HL}(\vec{I}_1 \cdot \vec{L})$$
(3)

We use the only time-dependent term $\Delta\omega\hat{L}_z$ to create a toggling frame $U(t)=\exp(-i\hat{L}_z\int_0^t\Delta\omega(t')\,dt')$. The corresponding Hamiltonian in this toggling frame is equation (4).

$$\begin{split} \widetilde{\mathcal{H}} &= U \left(\Delta \omega_0 \hat{L}_z + 2\pi J_{HH} (\vec{l}_1 \cdot \vec{l}_2) + 2\pi J_{HL} (\vec{l}_1 \cdot \vec{L}) \right) U^{\dagger} \\ &= \Delta \omega_0 \hat{L}_z + 2\pi J_{HH} (\vec{l}_1 \cdot \vec{l}_2) \\ &+ 2\pi J_{HL} \{ \hat{l}_{1z} \hat{L}_z + M(t) (\hat{l}_{1x} \hat{L}_x + \hat{l}_{1y} \hat{L}_y) + N(t) (\hat{l}_{1x} \hat{L}_y - \hat{l}_{1y} \hat{L}_x) \} \end{split} \tag{4}$$

in which $M(t)=\cos(\int_0^t\Delta\omega(t')\,dt')$, and $N(t)=\sin(\int_0^t\Delta\omega(t')\,dt')$. This toggling frame Hamiltonian has unveiled the physical picture of the pulse sequence. The role of the offset is to provide a small external magnetic field to the spins. The oscillating pulse then alters the form of the spin-spin interaction between the target nuclei and hydrides. The original flip-flop term, $\hat{I}_{1x}\hat{L}_x+\hat{I}_{1y}\hat{L}_y$, and the new interaction form, $\hat{I}_{1y}\hat{L}_x-\hat{I}_{1x}\hat{L}_y$, are tuned by the factors M(t) and N(t), respectively. These two terms connect the same states as the normal non-secular term, but with a $\pi/2$ phase shift of the off-diagonal operators, which will be clearer with the matrix form of the Hamiltonian shown later. When $T\to 0$, the oscillating pulse vanishes, and the system is recovered to continuous wave (CW) SABRE-SHEATH with M=1 and N=0.

For the square pulse (shown in Figure 1(a)) the zero-order average Hamiltonian is shown in equation (5).

$$\begin{split} \widetilde{\mathcal{H}}^{(0)} &= \frac{1}{T} \int_{0}^{T} \widetilde{\mathcal{H}}(t) dt \\ &= \Delta \omega_{0} \widehat{L}_{z} + 2\pi J_{HH} (\vec{I}_{1} \cdot \vec{I}_{2}) \\ &+ 2\pi J_{HL} \{ \widehat{I}_{1z} \widehat{L}_{z} + M_{0} (\widehat{I}_{1x} \widehat{L}_{x} + \widehat{I}_{1y} \widehat{L}_{y}) \\ &+ N_{0} (\widehat{I}_{1x} \widehat{L}_{y} - \widehat{I}_{1y} \widehat{L}_{x}) \} \end{split}$$
(5)

where $M_0=\frac{\sin(\theta)}{\theta}$, $N_0=\frac{1-\cos(\theta)}{\theta}$, and $\theta=\Delta\omega T/2$ representing the rotation angle in half a period is a function of pulse amplitude and pulse period. When θ is an integer multiple of 2π , both M_0 and N_0 go to zero, which means the coupling between hydrides and the target nuclei disappear at this situation, and no spin order transfer could take place.

A matrix expression of this zero-order Hamiltonian is powerful for providing physical insight. The basis used to express the matrix of the AA'B system is a singlet-triplet basis for the AA' pair and the Zeeman basis for the B spin. Equation (6) gives the two 3×3 subspaces of the zero-order Hamiltonian, which indicate that $M_0 \pm i N_0$ alter the interaction between the spin up states α_L and spin down states β_L of the target nuclei, and that the interaction strength only depends on its magnitude, $\sqrt{M_0^2 + N_0^2}$.

$$T_{H}^{*}\beta_{L} \qquad T_{H}^{*}\alpha_{L} \qquad S_{H}^{*}\alpha_{L} \qquad S_{H}^{*}\alpha_{L}$$

$$T_{H}^{*}\beta_{L} \qquad \frac{\pi (J_{HH} - J_{HL}) - \Delta \omega_{0}}{2} \qquad \frac{\pi J_{HL}}{\sqrt{2}} (M_{0} + iN_{0}) \qquad \frac{-\pi J_{HL}}{\sqrt{2}} (M_{0} + iN_{0})$$

$$T_{H}^{0}\alpha_{L} \qquad \frac{\pi J_{HL}}{\sqrt{2}} (M_{0} - iN_{0}) \qquad \frac{\pi J_{HL} + \Delta \omega_{0}}{2} \qquad \frac{\pi J_{HL}}{2}$$

$$T_{H}^{-}\alpha_{L} \qquad T_{H}^{0}\beta_{L} \qquad S_{H}^{0}\beta_{L}$$

$$T_{H}^{-}\alpha_{L} \qquad T_{H}^{0}\beta_{L} \qquad S_{H}^{0}\beta_{L}$$

$$T_{H}^{-}\alpha_{L} \qquad \frac{\pi (J_{HL} - J_{HL}) + \Delta \omega_{0}}{2} \qquad \frac{\pi J_{HL}}{\sqrt{2}} (M_{0} - iN_{0}) \qquad \frac{\pi J_{HL}}{\sqrt{2}} (M_{0} - iN_{0})$$

$$T_{H}^{0}\beta_{L} \qquad \frac{\pi J_{HL}}{\sqrt{2}} (M_{0} + iN_{0}) \qquad \frac{\pi J_{HL} - \Delta \omega_{0}}{2} \qquad \frac{-\pi J_{HL}}{2}$$

$$S_{H}^{0}\beta_{L} \qquad \frac{\pi J_{HL}}{\sqrt{2}} (M_{0} + iN_{0}) \qquad \frac{-\pi J_{HL}}{2}$$

While it would be possible to explicitly calculate higher order terms (S1 section 1) direct numerical evaluation of the full effective Hamiltonian gives a better comparison to test the validity. Each cycle of the square-pulse can be broken down into two constant fields, B_0+B and B_0-B , in time sequence. Labeling the corresponding time-independent Hamiltonians as \mathcal{H}_+ and \mathcal{H}_- , the propagator of this spin system is expressed as $U=\exp(-i\mathcal{H}_-T/2)\exp(-i\mathcal{H}_+T/2)=\exp(-i\bar{\mathcal{H}}T)$.

Extracting the average Hamiltonian by an expression such as $\overline{\mathcal{H}}=i\log(U)$ /T can be done numerically by diagonalizing U to a matrix $e^{i\Lambda}$, then taking the log of each eigenvalue (which will always have magnitude 1), $U = Ve^{i\Lambda}V^{\dagger}$; $\log U = V(i\Lambda)V^{\dagger}$, but this leads to a well-known ambiguity as the phase is only determined modulo 2π . This ambiguity is avoided by multiplying J_{HH} and J_{HL} by a scale factor α , calculating $\bar{\mathcal{H}}$ in the limit of very small α , and correcting for 2π phase jumps as α is increased to 1. This approach shows that the zero-order expansion is already a good approximation of the average Hamiltonian (Figure 3) so that higher order approximation can be neglected. M_0 , N_0 and $\sqrt{M_0^2 + N_0^2}$ (solid curves) calculated with the zero-order average Hamiltonian are in great agreement with their numerical counterparts (dashed curves). The coupling magnitude $\sqrt{M_0^2+N_0^2}$ vanishes at $\theta=2n\pi$, which agrees with the analytical expressions of M_0 and N_0 . $\sqrt{M_0^2 + N_0^2}$ attenuates as heta increases, in that it cannot fully recover to the previous maximum. The value of $\sqrt{M_0^2+N_0^2}$ is in the range of 0 to 1, which is obvious from the formula of M(t) and N(t)because they are conjugate trigonometric functions. In other words, the coupling between hydrides and the target nuclei can only be attenuated instead of being increased.

Unexpectedly, a diminished coupling strength yields much higher polarization. Figure 3(b) and (c) gives the relationship

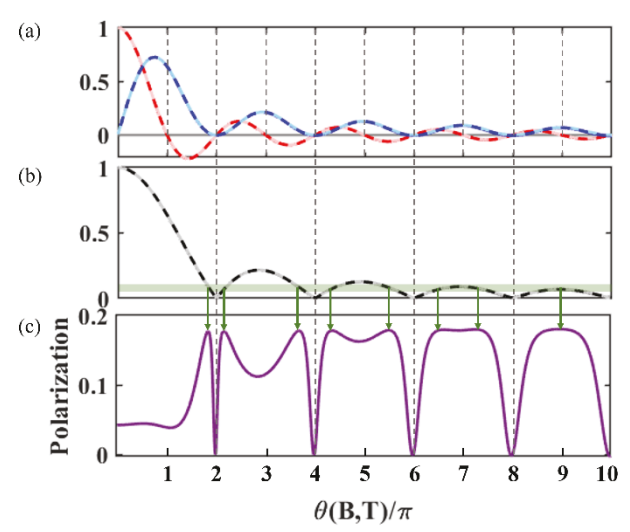
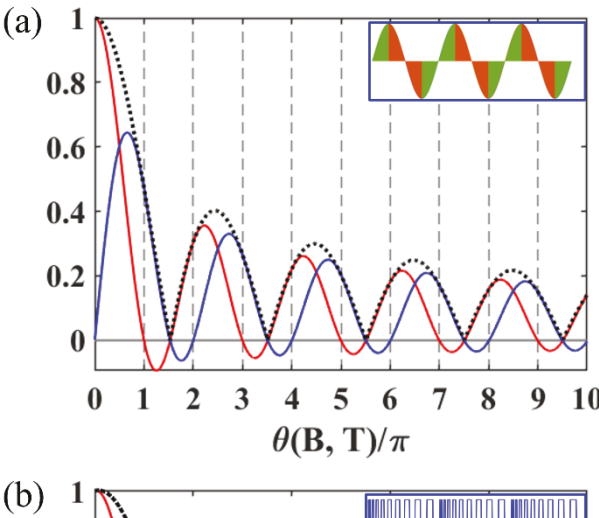
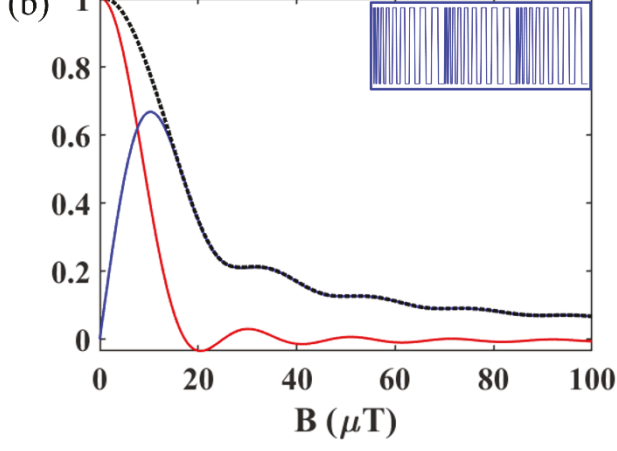


Fig. 3 (a) Curves of M and N as a function of θ/π . The solid lines (underlying bright red and bright blue curves) are the zero-order theoretical approximation of M and N, namely, M_0 and N_0 , and the dashed lines (light red and blue) are the exact values of M and N calculated with numerical method. (b) shows how the value of $\sqrt{M^2+N^2}$ varies with θ/π . Likewise, the solid curve (underlying black) and the dashed line (grey) correspond to the theoretical approximation and the numerical result, respectively. The horizontal green bar indicates the optimal value of $\sqrt{M^2+N^2}$. (c) Numerically simulated ^{15}N polarization of a 3-spin system with the pulse amplitude being fixed at $10\mu T$ and the offset being maintained at $-0.13\mu T$. The green arrows mark the maximum signals and their corresponding value of $\sqrt{M^2+N^2}$.

between the final polarization level and the value of $M_0^2+N_0^2$ with the offset field B_0 fixed at $-0.13\mu T$. The polarization is numerically simulated with the DMEx method, 28 and the dependence on θ indicates that when the interaction strength reduces to $M_0^2+N_0^2\sim 0.066$ (shown with a horizontal green bar in Fig. 3(b)), polarization is maximized. This unbalanced square wave indeed yields a large increase in signal. However, the optimal interaction strength $M_0^2+N_0^2\sim 0.066$ is very close to zero, and the polarization oscillations in Fig. 3 imply the large signals are not robust to imperfections of the pulse sequence such as inhomogeneity. This issue could be avoided if $M_0^2+N_0^2$ reduces gradually and does not periodically go to zero. To find a pulse sequence with this behaviour of $M_0^2+N_0^2$, more complex wave forms must be considered.

Figure 4(a) shows that M_0 , N_0 , and $\sqrt{M_0^2+N_0^2}$ of a sine wave have similar behaviours as they do for a square pulse. M_0 and N_0 in the zero-order average Hamiltonian are $M_0=\frac{1}{T}\int_0^T\cos\{\frac{\Delta\omega T}{2\pi}(1-\cos\frac{2\pi t}{T})\}dt$ and $N_0=\frac{1}{T}\int_0^T\sin\{\frac{\Delta\omega T}{2\pi}(1-\cos\frac{2\pi t}{T})\}dt$, and they periodically vanish at the same time. For all these sequences, the toggling frame is symmetric about the centre of each repeating interval (for example, the negative part of the square wave retraces back along the same trajectory followed in the positive part). In addition, both the square and sine wave have a symmetric trajectory with respect to the centre of each half cycle (depicted here as green and orange). This additional symmetry intuitively would be expected to produce cleaner pumping dynamics. However, it turns out that





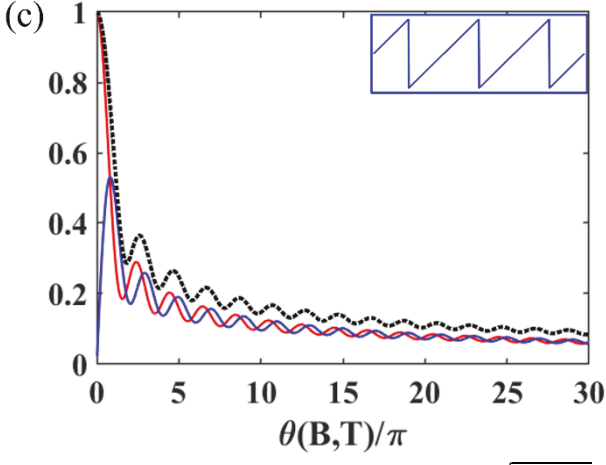


Fig. 4 Depiction of how M_0 (red curve), N_0 (blue curve) and $\sqrt{M_0^2+N_0^2}$ (black dotted curve) vary as a function of the rotation angle in half a period for a sine wave (a), a chirped square wave (b) and a sawtooth wave (c). We maintain the offset field at $-0.13\mu T$. As in Figure 3, frequent zero-crossings impose a serious constraint for the sine wave case on the usable fields, particularly if inhomogeneity is present, but not for the other cases.

this symmetry causes M_0 and N_0 to commonly go to zero simultaneously for the same value of the cycle length—a problem which is avoided by waveforms with lower symmetry (Fig. 1(c-d) and Fig. 4(b-c)).

To understand this effect, note that for an arbitrary oscillating pulse shape, M_0 and N_0 are given by

$$\begin{cases} M_0 = \frac{1}{T} \int_0^T M(t) dt = \frac{1}{T} \int_0^T \cos\left(\int_0^t \Delta \omega(t') dt'\right) dt \\ N_0 = \frac{1}{T} \int_0^T N(t) dt = \frac{1}{T} \int_0^T \sin\left(\int_0^t \Delta \omega(t') dt'\right) dt \end{cases}$$
(7)

which are integrals of the cosine and sine function of the instantaneous angle $\int_0^t \Delta\omega(t')dt'$, or in other words, integrals of the projections of a rotating unit vector on the x-axis and yaxis, respectively, in a rectangular coordinate system (Fig. 5). The trajectory of the unit vector in the first quarter of a period is plotted as the green area; in the second quarter the vector keeps moving clockwise but with inversely changing speed. Then the vector retraces its steps and completes a full period. Note that in both Fig. 3(a) and Fig. 4(a), zero crossings of M_0 occur with positive lobe areas of $(2n+1)\pi$ and zero crossings of N_0 occur at areas of $2n\pi$. These are simple symmetry effects, made clear by plotting the instantaneous values of M(t) and N(t) in the unit plane (Fig. 5). In general, the trajectory is symmetric about its midway point $\theta/2$, which fixes the ratio $N_0/M_0=\tan(\theta/2)$. For odd multiples of π $M_0=0$, and for even multiples $N_0 = 0$. Other than for those values of θ , the zero crossings of $M_{\rm 0}$ and $N_{\rm 0}$ depend on the details of the waveform. However, because the ratio between M_0 and N_0 is fixed, zeroes at any θ value must coincide, giving zero efficiency for generating polarization. Thus, any waveform which has this symmetry (or can be given this symmetry by a time shift and a

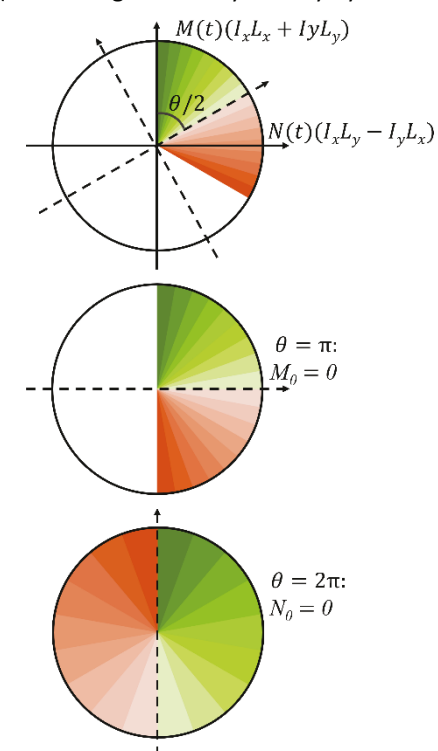


Fig. 5 For many common waveforms (such as a sine or square wave) the time-dependent rotation between (xx+yy) and (xy-yx) terms is antisymmetric about the midpoint, and each lobe is symmetric. In this case, the relative values of the average coefficients of these two terms (M_0 and N_0 respectively) is constrained by symmetry to be along an axis with half the rotation angle of each lobe. Except for the special cases $\theta=n\pi$, this means that zeroes in M_0 and N_0 must coincide, creating values which generate no polarization.

amplitudes but the same area in the positive and negative lobes), the enforced simultaneity of M_0 and N_0 zero crossings creates a highly structured pumping profile. In contrast, the lower symmetry in Fig. 4(b)-(c) avoids simultaneous zeroes. Fig. 1(c) and 4(b) show a chirped pulse with evenly growing wavelength in each period, τ_0 , $\tau_0 + \Delta \tau$, ... $\tau_0 + m \Delta \tau$, and $\sum_{j=0}^{m} (\tau_0 + j\Delta \tau) = T$. The chirped pulse we use here has $\tau_0 =$ $\Delta \tau = 0.2 ms. \ \sqrt{M_0^2 + N_0^2}$ of this pulse is close to the optimal value 0.066 when the pulse amplitude B is larger than $40\mu T$, accordingly the resulting experimental robustness to the pulse amplitude is indeed improved. We finally try an asymmetric pulse shape, a ramp pulse (Figure 1(d)), which turns out to be robust to both the pulse period and the field strength. The analytical solution of a ramp pulse is similar to equation (5), except that M_0 and N_0 are replaced by $M_0 =$ $rac{2}{\sqrt{\Delta\omega T}}\int_0^{\sqrt{\Delta\omega T}/2}\cos\!x^2dx$, and $N_0=rac{2}{\sqrt{\Delta\omega T}}\int_0^{\sqrt{\Delta\omega T}/2}\sin\!x^2dx$. Unlike the square pulse and sine wave whose effective J_{HL} coupling

prepulse, such as an unbalanced square wave with different

the square pulse and sine wave whose effective J_{HL} coupling can be fully averaged out when M and N become zero at the same time. The ramp wave successfully avoids zero points. Because the coupling strength $\sqrt{M_0^2+N_0^2}$ gradually approaches zero as the pulse period or pulse amplitude increase (namely $\theta(B,T)$ increases), in a wide period and amplitude domain it always stays close to the optimal value 0.066, indicated in Figure 4(c).

For continuous wave excitation in SABRE/X-SABRE, we recently pointed out 23 that the level anticrossing $^{12,\ 29\text{-}32}$ condition does not even give qualitatively correct predictions except for very small J_{HL} couplings and very slow exchange. For example, in the case of the AA'B system shown in Fig. 2(a) with $J_{HH}=-8Hz$, and $J_{HL}=-25Hz$ in a continuous low magnetic field, the LAC occurs at $\pm 0.04\mu T$ which is far from the experimental optimum $\pm 0.6\mu T$. The failure of the level anticrossing condition here is mainly because it oversimplifies a 3×3 (or larger) subspace to a 2×2 space and usually cannot accurately account for the dynamics of the original system. Interestingly, though, the LAC condition becomes more relevant for oscillating pulse SABRE/X-SABRE, because the oscillating pulses reduce the off-diagonal elements in equation (6) but not the diagonal ones, thus improving the separation from unwanted states.

Fig. 6 depicts how the energy levels of the first subspace in equation (6) vary with the offset field. The subfigure 6(a) relates

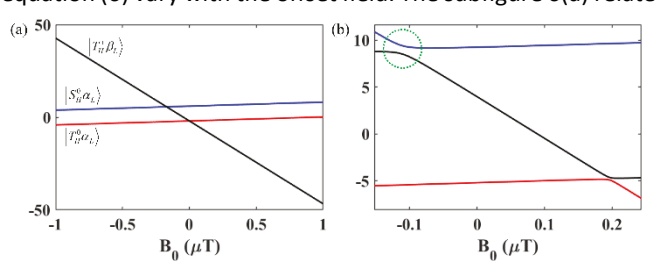


Fig. 6 Eigenvalues as a function of the offset field. (a) corresponds to the case of $J_{HL}=0$, while (b) refers to the case of optimal interaction $J_{HL}=-25 \, \mathrm{Hz}$ and $\sqrt{M_0^2+N_0^2}\sim 0.066$.

to $J_{HL}=0$, and no LACs occur because there is no interaction between the states. While Fig. 6(b) refers to the case of optimal interaction $J_{HL}=-25 \, \mathrm{Hz}$ and $\sqrt{M_0^2+N_0^2}\sim 0.066$, in which the circled LAC is in great agreement with the optimal offset filed $\pm 0.13 \mu T$.

Results and Discussion

In this section, we verify the analytical results above with both simulations and experiments. All Simulations are done with the DMEx method²⁸ which is a recently developed numerical modelling approach for exchanging systems and has shown robust agreement with experimental results. All oscillating pulse SABRE-SHEATH experiments were performed by bubbling 43% parahydrogen through a methanol-d4 solution under 7 bars of pressure at room temperature. The SABRE sample used here was prepared by adding ¹⁵N-acetonitrile (50mM), natural-abundance ¹⁴N-pyridine (25mM), and the catalyst precursor [IrCl(COD)(IMes)] (4.4 mM) into 500µL deuterated methanol solvent. The catalyst was first activated by bubbling hydrogen

gas through the SABRE sample for 30-60min to generate SABRE complex $[IrH_2(^{15}N-Py)_2(IMes)]^+(^{15}N-py) = ^{15}N-pyridine)$. The whole sample was then bubbled for 60s inside a solenoid coil within a μ -metal magnetic shield in which the polarization transfer occurs. We connect the solenoid coil to a function generator to create different oscillating fields inside the coil. Finally, the sample was manually transferred (1-2s) to a 1 Tesla ^{15}N Magritek NMR spectrometer for detection.

We start with the square pulse sequence (Fig. 7(a)). The 3D plot Fig. 7(a1) shows how the final polarization varies with the pulse period and the offset field while the pulse amplitude is fixed at $10\mu T$. The optimal offset field here is around $\sim 0.13\mu T$ rather than $\sim 0.6\mu T$ in the CW SABRE-SHEATH case even though the oscillating pulse has nothing to do with the Zeeman terms of the spin system. Besides, at the points T=20.8ms, and T=25~ms which make $\theta=2n\pi$, no polarization is produced. All the analysis based on theory is in accordance with the experimental results. Figure 7(b) shows the polarization of a sine wave pulse as a function of both the pulse period and the

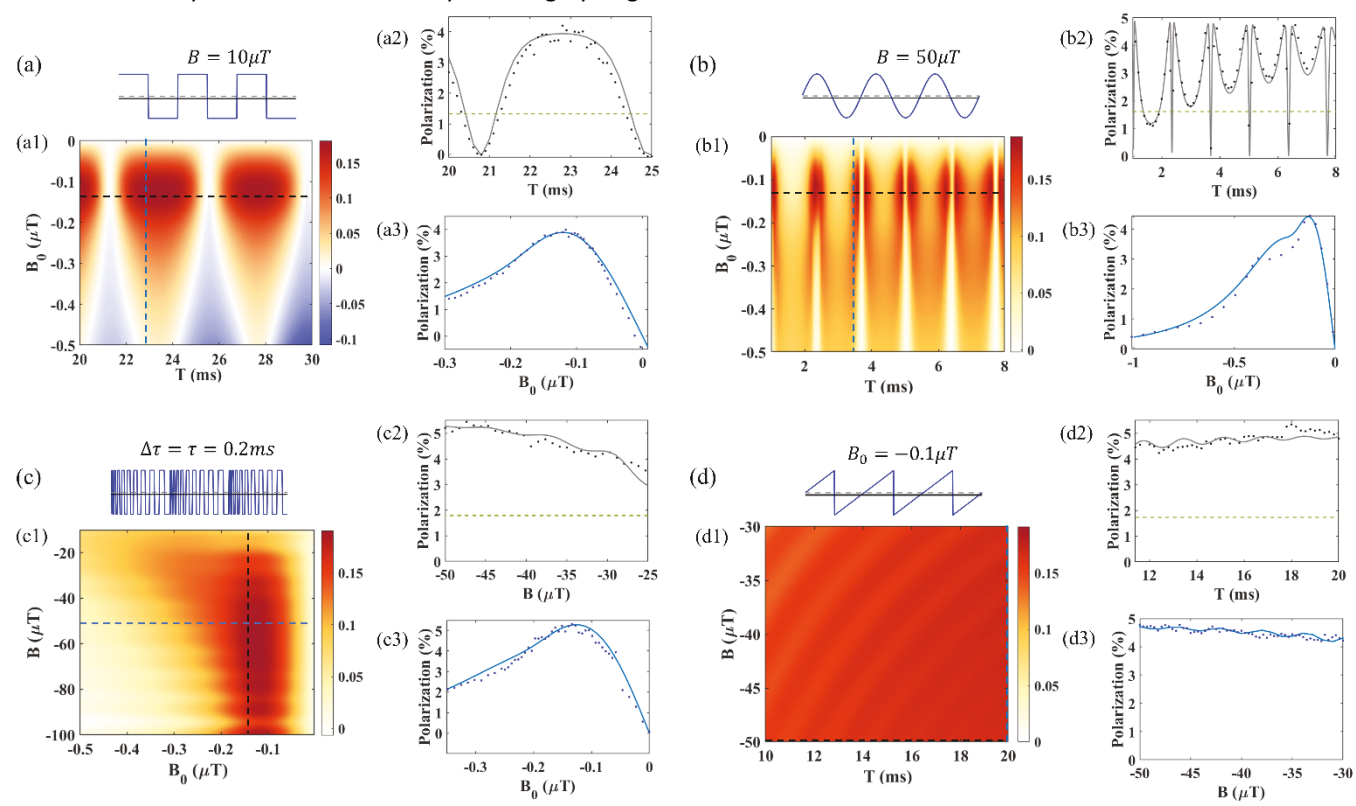


Fig. 7 Experimental validation of theoretical predictions. (a) Square pulse (a1) Theoretical effects of a square pulse sequence with a fixed amplitude $B=10\mu T$ and various pulse periods and offset fields. (a2) Comparison of theoretical calculations with experimental data holding $B_0=-0.13\mu T$ and varying T. (a3) Comparison of theoretical calculations with experimental data holding $B_0=-0.13\mu T$ and varying T. (b3) Comparison of theoretical calculations with experimental data holding $B_0=-0.13\mu T$ and varying T. (b3) Comparison of theoretical calculations with experimental data holding $B_0=-0.13\mu T$ and varying T. (b3) Comparison of theoretical calculations with experimental data holding $B_0=-0.13\mu T$ and varying $B_0=0.25\mu T$ and

offset field while the pulse amplitude is maintained at 50µT. We varied either the pulse period $(1ms \le T \le 8ms, B_0 =$ $-0.13\mu T$) in Fig. 7(b2), or the offset field $(-1\mu T \le B_0 \le 0\mu T$, T=3.5ms) in Fig. 7(b3). In agreement with the theoretical predictions, the final polarization periodically reduces to zero at a frequency corresponding to $\Delta\omega$, and the optimal pulse periods come close to zero polarization points. The optimal offset field is also shifted from $\sim 0.6 \mu T$ to $\sim 0.13 \mu T$. The result of a chirped pulse is displayed in Figure 7(c). Provided the offset is maintained in the range from $-0.18\mu T$ to $-0.08\mu T$, the polarization is robust to all pulse amplitudes larger than $40\mu T$ and stays within the range from 16.5% to 19%. The last oscillating pulse, ramp pulse, is shown in Fig. 7(d). By varying the pulse period and amplitude while fixing the offset field at $-0.1\mu T$, the simulation result, Fig. 7(d1), clearly shows that in a fairly wide range of both the pulse period and the pulse amplitude the final polarization always stays close to the maximum, which has been confirmed by experiments, Fig. 7(d2) and 7(d3). By varying either the pulse period ($11ms \le T \le$ $20ms,~B=50\mu T,~B_0=-0.1\mu T)$ or the pulse amplitude $(30\mu T \le B \le 50\mu T, T = 20ms, B_0 = -0.1\mu T)$, we always obtained almost maximum polarization. The signal enhancement of these oscillation pulse sequences is as high as 300%.

Robustness to Exchange Rate

In this section, we use the DMEx simulation method²⁸ to demonstrate that oscillating pulse SABRE-SHEATH is fairly robust to variations of exchange rate. We use the same square pulse in Fig. 2 and calculate the polarization, varying the exchange rate by a factor of 100. In the case of low substrate exchange rate (Fig. 8(a) and (b)), the optimal condition stays around $B_0 = -0.11 \mu T$, T = 4.1ms. Ultimately, as the exchange

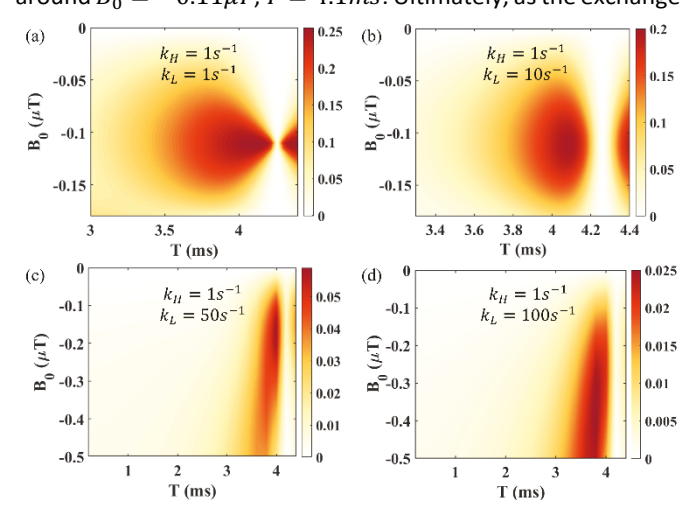


Fig. 8 Different optimal polarization conditions caused by different exchange rates of substrate. (a) $k_H=1s^{-1},\ k_L=1s^{-1},$ the optimal field is -0.11μT, and the optimal period is 4.12ms. (b) $k_H=1s^{-1},\ k_L=10s^{-1},$ the optimal field is -0.11μT, and the optimal period is 4.08ms. (c) $k_H=1s^{-1},\ k_L=50s^{-1},$ the optimal field is -0.17μT, and the optimal period is 4.0ms. (d) $k_H=1s^{-1},\ k_L=100s^{-1},$ the optimal field is -0.37μT, and the optimal period is 3.8ms. The four subplots have inconsistent color scales in order to show off more detail.

rate of the substrate goes up, the optimal condition shifts in the direction so that the optimal offset field increases and the pulse period decreases. Here we give an explanation with the quantum dynamics of SABRE. Fig. 9 shows the polarization of the target nuclei as a function of the quantum evolution time. Both chemical exchange and relaxation processes are neglected. The four curves in Figure 9 depicts the quantum dynamics using optimal parameters B₀ and T for the four cases of Fig. 8, respectively. The red and blue curves clearly show that under the condition $B_0 = -0.11 \mu T$ and T = 4.1 ms, the polarization of the target nuclei could be raised up to 80%. However, when the chemical exchange processes are included, the quantum evolution is interrupted, which means the spin order transfer is interrupted. On one hand, if the lifetime of the SABRE complex is long, for example $k_L = 1s^{-1}$ or $k_L = 10s^{-1}$, there is enough time that the target nuclei could be polarized before they dissociate from SABRE catalyst. On the other hand, during a short lifetime, say $k_L = 50s^{-1}$ or $k_L = 100s^{-1}$, substantial spin order transfer cannot be completed. A smaller but faster polarization transfer process works better (the green and black curves). As pulse period T decreases, the value of $\sqrt{M^2 + N^2}$ grows, and the coupling between the hydrides and the target nuclei increases accordingly, which causes the spin order transfer faster (shown in Fig. 9(b)). For a fixed pulse period T, there exists an optimal offset field which maximizes the polarization of the substrate. In conclusion, maximizing SABRE polarization is a trade-off between the speed of spin order transfer and the largest transfer degree. Usually, the exchange rate k_L is in the range from $5s^{-1}$ to $50s^{-1}$, and the corresponding optimal condition remains near $B_0 = -0.11 \mu T$ and T=4.1ms, (see Fig. 8(b) and (c)). Even if the optimal

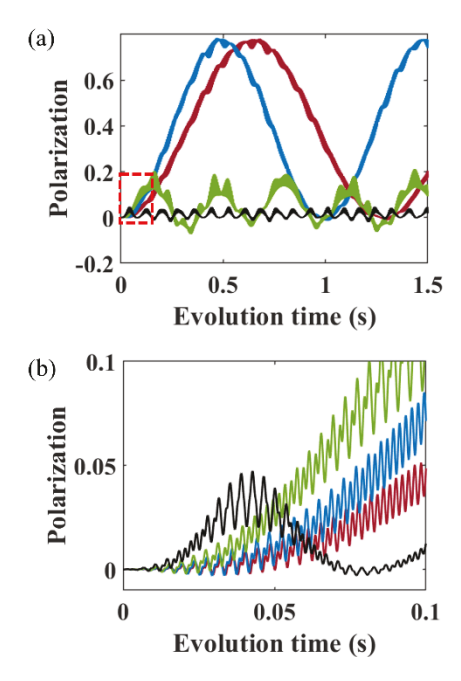


Fig. 9 (a) Polarization generated by quantum evolution of the 3-spin system. red curve $B_0=-0.11\mu T$, T=4.12ms; blue curve $B_0=-0.11\mu T$, T=4.08ms; green curve $B_0=-0.17\mu T$, T=4.0ms; black curve $B_0=-0.31\mu T$, T=3.8ms. (b) A zoomed-in version of the red box in figure (a). As the period goes down the spin order transfer process speeds up.

condition shifts, for example, Fig. 8(d), the polarization (1.4%) generated by an oscillating pulse with $B_0=-0.11\mu T$ and T=4.1ms is still larger than the maximum signal (0.2%) produced by CW SABRE-SHEATH method. This robustness to exchange rate is also extended to AA'BB' system and a positive JHH situation (SI section 5).

Conclusions

We have shown, in both experiments and simulations, that a variety of oscillating magnetic fields can significantly improve SABRE-SHEATH hyperpolarization, relative to a continuous field or even one pulsed to optimize polarization transfer. In effect, the interactions between hydrides and target nuclei are adjustable by tuning the pulse amplitude, pulse period, and pulse shape. As described above, we improve the robustness to experimental imperfections by exploring different pulse shapes. Finally, it turns out that a pulse shape with reduced symmetry, such as a ramp wave, generates significant improvements in achievable polarization and is robust to experimental imperfection.

In this work, the largest polarization yielded with 43% parahydrogen is ~5.3%; this would correspond to 22% polarization with 100% parahydrogen. In our simulations, the maximum polarization generated by SABRE-SHEATH method is as high as 80% (with 100% parahydrogen). However, in reality, polarization is limited by the low accessibility of parahydrogen or slow refresh rate of the dissolved hydrogen in the SABRE solvent. This gap between principle and reality indicates that SABRE retains room for improvement. Still, our approach is technologically simple, capable of producing significant enhancements, and suggests there is still room for further pulse sequence exploration.

Author Contributions

Conceptualization: XL, WSW, JRL, SLE

Methodology: XL Software: XL Investigation: XL Visualization: XL, WSW Supervision: WSW

Writing—original draft: XL, WSW

Writing—review & editing: XL, WSW, JRL, SLE

Conflicts of interest

There are no conflicts to declare.

Acknowledgements

This work was supported by the National Science Foundation under grant CHE-2003109

Notes and references

- J. H. Ardenkjaer-Larsen, B. Fridlund, A. Gram, G. Hansson, L. Hansson, M. H. Lerche, R. Servin, M. Thaning, K. Golman, *Proc. Natl. Acad. Sci. U.S.A.*, 2003, **100**, 10158.
- 2 T. G. Walker and W. Happer, *Reviews of modern physics*, 1997, **69**. 629.
- T. C. Eisenschmid, R. U. Kirss, P. P. Deutsch, S. I. Hommeltoft, R. Eisenberg, J. Bargon, R. G. Lawler, A. L. Balch, J. Am. Chem. Soc., 1987, 109, 8089.
- 4 C. R. Bowers, D. P. Weitekamp, J. Am. Chem. Soc. 1987, 109, 5541.
- 5 R. W. Adams, J. A. Aguilar, K. D. Atkinson, M. J. Cowley, P. I. P. Elliott, S. B. Duckett, G. G. R. Green, I. G. Khazal, J. Lopez-Serrano, D. C. Williamson, *Science.*, 2009, 323, 1708.
- 6 K. D. Atkinson, M. J. Cowley, P. I. P. Elliott, S. B. Duckett, G. G. R. Green, J. Lopez-Serrano, A. C. Whitwood, J. Am. Chem. Soc., 2009, 131, 13362.
- L. D. Vazquez-Serrano, B. T. Owens, J. M. Buriak, *Inorg. Chim. Acta*, 2006, **359**, 2786.
- M. J. Cowley, R. W. Adams, K. D. Atkinson, M. C. R. Cockett, S.
 B. Duckett, G. G. R. Green, J. A. B. Lohman, R. Kerssebaum, D.
 Kilgour, R. E. Newis, J. Am. Chem. Soc., 2011, 133, 6134.
- 9 T. Theis, M. L. Truong, A. M. Coffey, R. V. Shchepin, K. W. Waddell, F. Shi, B. M. Goodson, W. S. Warren, E. Y. Chekmenev, J. Am. Chem. Soc., 2015, 137, 1404.
- 10 M. L. Truong, T. Theis, A. M. Coffey, R. V. Shchepin, K. W. Waddell, F. Shi, B. M. Goodson, W. S. Warren, E. Y. Chekmenev, J. Phys. Chem. C., 2015, 119, 8786-97.
- 11 J. R. Lindale, S. L. Eriksson, C. P. N. Tanner, Z. Zhou, J. F. P. Colell, G. Zhang, J. Bae, E. Y. Chekmenev, T. Theis, W. S. Warren, *Nature Communication*, 2019, **23**.
- 12 A. N. Pravdivtsev, A. V. Yurkovskaya, N. N. Lukzen, H.-M. Vieth, K. L. Ivanov, *Phys. Chem. Chem. Phys.*, 2014, **16**, 24672-24675.
- 13 T. Theis, M. L. Truong, A. M. Coffey, E. Y. Chekmenev, W. S. Warren, *J. Magn. Reson.*, 2014, **248**, 23.
- 14 J. R. Lindale, C. P. Tanner, S. L. Eriksson, W. S. Warren, *J. Magn. Reason.*, 2019, **307**, 106577.
- 15 S. S. Roy, G. Stevanato, P. J. Rayner, S. B. Duckett, *J. Magn. Reason.*, 2017, **285**, 55-60.
- 16 S. Knecht, A. S. Kiryutin, A. V. Yurkovskaya, K. L. Ivanov, Molecular Physics, 2019, 117, 2762-2771.
- 17 M. E. Gemeinhardt, M. N. Limbach, T. R. Gebhardt, C. W. Eriksson, S. L. Eriksson, J. R. Lindale, E. A. Goodson, W. S. Warren, E. Y. Chekmenev, B. M. Goodson, *Angew. Chem.*, 2020, **59**, 418-423.
- 18 N. M. Ariyasingha, J. R. Lindale, S. L. Eriksson, G. P. Clark, T. Theis, R. V. Shchepin, N. V. Chukanov, K. V. Kovtunov, I. V. Koptyug, W. S. Warren, *The journal of physical chemistry letters*, 2019, **10**, 4229-36.
- 19 M. J. Burns, P. J. Rayner, G. G. Green, L. A. Highton, R. E. Mewis, S. B. Duckett, *The Journal of Physical Chemistry B.*, 2015, **119**, 5020-7.
- 20 V. V. Zhivonitko, I. V. Skovpin, I. V. Koptyug, *Chemical Communications*, 2015, **51**, 2506-2509.
- 21 J.-B. Hçvener, A. N. Pravdivtsev, B. Kidd, C. R. Bowers, S. Glçggler, K. V. Kovtunov, M. Plaumann, R. Katz-Brull, K. Buckenmaier, A. Jerschow, F. Reineri, T. Theis, R. V. Shchepin, S. Wagner, P. Bhattacharya, N. M. Zacharias, E. Y. Chekmenev, Angew. Chem. Int. Ed., 2018, 57, 11140 11162; Angew. Chem., 2018, 130, 11310 11333.
- 22 J. F. Colell, A. W. Logan, Z. Zhou, R. V. Shchepin, D. A. Barskiy, Jr G. X. Ortiz, Q. Wang, S. J. Malcolmson, E. Y. Chekmenev, W. S. Warren, *The Journal of Physical Chemistry C*, 2017, 121, 6626-34
- 23 S. L. Eriksson, J. R. Lindale, X. Li, W. S. Warren, *Sci. Adv.*, 2022, 8, 11. arXiv:2107.04687

- 24 L. Dagys, C. Bengs, M. H. Levitt, *J. Chem. Phys.*, 2021, **155**, 154201.
- 25 A. N. Pravdivtsev, N. Kempf, M. Plaumann, J. Bernarding, K. Scheffler, J. -B. Hövener, K. Buckenmaier, *ChemPhysChem* 2021, **22**, 2379.
- 26 U. Haeberlen, J. S. Waugh, *Phys. Rev.*, 1968, **175**, 453.
- 27 U. Haeberlen, *High Resolution NMR in Solids*, Academic, New York, 1976.
- 28 J. R. Lindale, S. L. Eriksson, C. P. N. Tanner, W. S. Warren, *Sci. Adv.*, 2020, **6**, 32.
- 29 A. N. Pravdivtsev, A. V. Yurkovskaya, H.-M. Vieth, K. L. Ivanov, R. Kaptein, *ChemPhysChem*, 2013, **14**, 3327 3331.
- 30 L. D. Landau, Zur theorie der energieubertragung ii. Z. Sowjetunion, 1932, **2**, 46-51.
- 31 K. L. Ivanov, A. N. Pravdivtsev, A. V. Yurkovskaya, H.-M. Vieth, R. Kaptein, *Progress in nuclear magnetic resonance spectroscopy*, 2014, **81**, 1-36.
- 32 B. A. Rodin, K. L. Ivanov, *Magnetic Resonance*, 2020, **1**, 347-